

Interpenetrating Triphase Cobalt-Based Nanocomposites as Efficient Bifunctional Oxygen Electrocatalysts for Long-Lasting Rechargeable Zn–Air Batteries

Yi Jiang, Ya-Ping Deng, Jing Fu, Dong Un Lee, Ruilin Liang, Zachary Paul Cano, Yangshuai Liu, Zhengyu Bai,* Sooyeon Hwang, Lin Yang, Dong Su, Weiguo Chu,* and Zhongwei Chen*

Rational construction of atomic-scale interfaces in multiphase nanocomposites is an intriguing and challenging approach to developing advanced catalysts for both oxygen reduction (ORR) and evolution reactions (OER). Herein, a hybrid of interpenetrating metallic Co and spinel Co_3O_4 “Janus” nanoparticles stitched in porous graphitized shells ($\text{Co}/\text{Co}_3\text{O}_4@\text{PGS}$) is synthesized via ionic exchange and redox between Co^{2+} and 2D metal–organic–framework nanosheets. This strategy is proven to effectively establish highways for the transfer of electrons and reactants within the hybrid through interfacial engineering. Specifically, the phase interpenetration of mixed Co species and encapsulating porous graphitized shells provides an optimal charge/mass transport environment. Furthermore, the defect-rich interfaces act as atomic-traps to achieve exceptional adsorption capability for oxygen reactants. Finally, robust coupling between Co and N through intimate covalent bonds prohibits the detachment of nanoparticles. As a result, $\text{Co}/\text{Co}_3\text{O}_4@\text{PGS}$ outperforms state-of-the-art noble-metal catalysts with a positive half-wave potential of 0.89 V for ORR and a low potential of 1.58 V at 10 mA cm^{-2} for OER. In a practical demonstration, ultrastable cyclability with a record lifetime of over 800 h at 10 mA cm^{-2} is achieved by Zn–air batteries with $\text{Co}/\text{Co}_3\text{O}_4@\text{PGS}$ within the rechargeable air electrode.

1. Introduction

Rechargeable metal–air batteries are considered as one of the most promising energy storage systems because of their high theoretical energy density, low cost, and improved safety.^[1–3] However, their inferior energy conversion efficiency and low lifetimes are the main bottlenecks limiting their widespread applications.^[4,5] These shortcomings predominantly originate from the intrinsically sluggish kinetics of the oxygen reduction (ORR) and evolution (OER) reactions, as well as their limited stability in harsh alkaline electrolytes.^[6–8] To address the above issues, much effort has been devoted to the exploration of active and durable bifunctional electrocatalysts.^[9–12]

Although noble-metal catalysts, such as platinum (Pt), ruthenium (Ru), iridium (Ir), and their alloys, are regarded as the best-known oxygen electrocatalysts, their commercialization has been greatly hindered

Y. Jiang, Prof. W. Chu
CAS Key Laboratory for Nanosystem and Hierarchical Fabrication
CAS Center for Excellence in Nanoscience
National Center for Nanoscience and Technology
Beijing 100190, P. R. China
E-mail: wgchu@nanoctr.cn

Y. Jiang, Prof. W. Chu
University of Chinese Academy of Sciences
Beijing 100049, P. R. China

Y. Jiang, Y.-P. Deng, J. Fu, D. U. Lee, R. Liang, Z. P. Cano, Y. Liu,
Prof. Z. Chen
Department of Chemical Engineering
Waterloo Institute for Nanotechnology
Waterloo Institute for Sustainable Energy
University of Waterloo
Waterloo, Ontario N2L 3G1, Canada
E-mail: zhwen@uwaterloo.ca

Prof. Z. Bai, Prof. L. Yang
School of Chemistry and Chemical Engineering
Henan Normal University
Xinxiang 453007, China
E-mail: baizhengyu2000@163.com

S. Hwang, Prof. D. Su
Center for Functional Nanomaterials
Brookhaven National Laboratory
Upton, NY 11953, USA

 The ORCID identification number(s) for the author(s) of this article can be found under <https://doi.org/10.1002/aenm.201702900>.

DOI: 10.1002/aenm.201702900

by their insufficient catalytic bifunctionality, scarcity and high cost.^[13,14] Therefore, the pursuit of earth-abundant and low-cost electrocatalysts with excellent bifunctionality and stability is necessary to realize the commercialization of rechargeable metal–air batteries.^[15–20] The transition metal oxides, especially spinel Co_3O_4 , have been explored as promising alternatives to noble-metal catalysts owing to their relatively abundant reserves and theoretically high catalytic activity.^[21–26] However, their inferior electrical conductivity hinders charge injection to and extraction from O_2 , which limits the catalytic activity of the semiconducting Co_3O_4 catalysts. Conductive carbon coating on Co_3O_4 is an effective strategy to facilitate surface charge transfer in the obtained hybrid electrocatalysts.^[27–30] Metals incorporations have also been reported to facilitate faster charge transport inside the electrocatalyst phase, despite of their incapability to catalyze OER.^[13] Consequently, optimizing the charge transfer both inside and on the surface of Co_3O_4 maximizes the utilization of active sites, and further raises the efficiency of metal–air batteries.^[31,32]

One critical criterion for this method is the phase interface present in a composite, which leads to lattice defects that enhance electron transfer efficiency of such heterostructured Co particles.^[33,34] Moreover, the lattice defects would also create extra active sites.^[28] Currently, these hybrid materials consist of phases in which one functional component is simply coated or coupled to another, usually the structural combination.^[35,36] However, they have their own limitations at the present stage, namely, the low interconnectivity and physical distinctions between different phases, which greatly hinders the desired bifunctional oxygen electrocatalytic activity and stability. Therefore, constructing an interpenetrating conjunction among the metal, spinel, and carbon at atomic-scale is vital to enhance the activity and durability, but has yet to be achieved.

Although direct carbonization of Co metal–organic-frames (Co MOFs), $[\text{Co}(\text{2-methylimidazole})_2]_n$, is commonly adopted to synthesize Co-based electrocatalysts,^[37–41] this method cannot control the chemical state of Co species that would inevitably reduce to metallic Co. The metallic Co produced would in turn catalyze the graphitization of organic ligands in Co MOFs, subsequently reduces the degree of porosity and N content of the final product.^[42] In comparison, carbon materials obtained via pyrolysis of Zn MOFs, $[\text{Zn}(\text{2-methylimidazole})_2]_n$, exhibit relatively high porosity and N contents,^[43] but their amorphousness limits charge diffusion in electrocatalytic processes. Zn MOFs may be considered as an ideal scaffold to immobilize Co^{2+} ions through coordination interaction with the exposed unsaturated sites on surface.^[44] Therefore, it is anticipated that controllably incorporating Co^{2+} into Zn MOFs would not only integrate the merits of abundant N content and graphitization, but also allows precise tuning of the reductive degree of the Co species.

Herein, a novel catalyst design to improve catalyst performance is shown. This design is centered on constructing a hybrid of interpenetrating metallic Co and spinel Co_3O_4 “Janus” nanoparticles stitched in porous graphitized shells ($\text{Co}/\text{Co}_3\text{O}_4@$ PGS). This hybrid catalyst possesses unique nanoscale dimensions and functionalities, three different phases, metal, spinel, and carbon, that are topologically interconnected throughout the nanostructures. By constructing the interpenetrating

triphasic features, i.e., atom trapping defective interfaces and porous graphitized shell, beneficial for charge transfer and active site utilization are incorporated into the catalyst. As a result, the $\text{Co}/\text{Co}_3\text{O}_4@$ PGS catalyst showed significantly improved catalytic and electrochemical performance, outperforming state-of-the-art benchmark noble-metal catalysts and other recently reported bifunctional catalysts. Moreover, the robust covalent bonds between Co and N within the hybrid are keys to prevent detachment of nanocrystals from PGS. These advantages combine to bring substantial activity and durability improvements to the as-prepared $\text{Co}/\text{Co}_3\text{O}_4@$ PGS for both ORR and OER. As a practical demonstration, a low charge–discharge gap and a record rechargeable lifetime lasting over 800 h are achieved when integrating $\text{Co}/\text{Co}_3\text{O}_4@$ PGS into the air electrode of a Zn–air battery.

2. Results and Discussion

2.1. Synthesis and Characterization

With the aim of obtaining $\text{Co}/\text{Co}_3\text{O}_4@$ PGS, the novel chemical-state controlled strategy based on single Zn MOF nanosheets is illustrated in **Figure 1**. Zn MOFs are first synthesized by mixing Zn nitrate hexahydrate and 2-methylimidazole in an aqueous solution at room temperature. Zn MOFs are then reacted with cobalt nitrate hexahydrate in ethanol. In this process, Co^{2+} precursors are incorporated into the Zn MOFs via two routes: one is the formation of coordination bonds between Co^{2+} and unsaturated N-atom groups on the Zn MOF surface, and the other is the cation exchange between Co^{2+} and Zn^{2+} in the Zn MOFs matrix owing to the stronger coordination ability of Co^{2+} compared to Zn^{2+} .^[45] As the reaction occurs, the color of the precursor (Zn/Co MOFs- $\text{Co}(\text{NO}_3)_2$) changes from white to pinkish purple (Figure S1a,b, Supporting Information), indicating the Co^{2+} ions are successfully incorporated into Zn MOFs. The coordination bonds between Co^{2+} and N-atom groups are experimentally confirmed by infrared (IR) spectroscopy, which shows a slightly red shift of the metal–N peak to 422 cm^{-1} (Figure S1c, Supporting Information).^[46] Additionally, a new peak at 1384 cm^{-1} appeared in the IR spectrum for precursor of Zn/Co MOF- $\text{Co}(\text{NO}_3)_2$ corresponding to the N–O bonds in Co (II) nitrate (Figure S1c, Supporting Information).^[47] The final product ($\text{Co}/\text{Co}_3\text{O}_4@$ PGS) is obtained by pyrolyzing the precursor with a Co^{2+} to Zn MOFs ratio (δ) of 1.5 under argon gas flow. During this process, Co (II) nitrate adsorbed on the MOFs surface could be converted and further oxidized to Co_3O_4 by the nitrate anions with oxidizing ability. Meanwhile, the Co^{2+} ions within the MOFs matrix through the coordination with unsaturated N-atom groups are reduced to the metallic state through a redox reaction with the organic ligands.^[48] Therefore, an intimate heterogeneous mixture of Co_3O_4 and metallic Co may be obtained, and the relative proportions of Co chemical states can be altered with different δ values in the precursors. As control experiments, species without Co and with differing degrees of Co reduction during the one-step pyrolysis are obtained and denoted as carbon nanosheets (CNS) ($\delta = 0$), $\text{Co}@$ PGS ($\delta = 1.0$), and $\text{Co}_3\text{O}_4@$ PGS ($\delta = 2.0$).

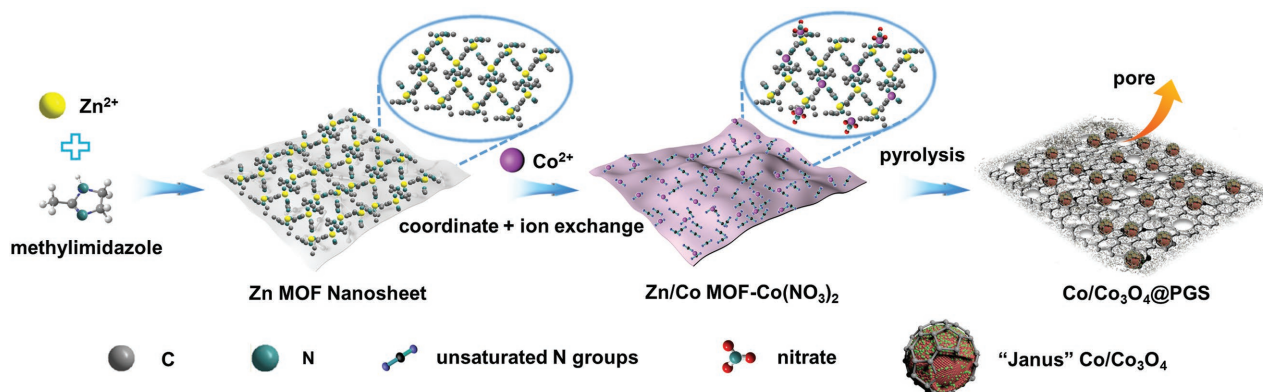


Figure 1. Illustration of synthesis process used to prepare interpenetrating Co and Co_3O_4 nanoparticles stitched in porous graphitized shells ($\text{Co}/\text{Co}_3\text{O}_4@PGS$). In “Janus” nanoparticles, the red part represents metallic Co and the green part represents Co_3O_4 .

The detailed pyrolysis process has been revealed by thermogravimetric analysis (TGA) as follows (Figure S2, Supporting Information). First, a slight weight loss at around $300\text{ }^\circ\text{C}$ occurred due to thermal decomposition of Co (II) nitrate to Co oxides at the surface of MOFs.^[48] Then, with increasing temperature, another weight loss in the region of $500\text{--}600\text{ }^\circ\text{C}$ is observed as the MOFs undergo carbonization. In this process, the organic ligands of MOFs oxidized to carbon atoms or carbon monoxide/dioxide, accompanied by the controllable reduction of a portion of metal ions into the metallic state. Finally, beyond $900\text{ }^\circ\text{C}$, a slight weight loss is observed due to the evaporation of Zn atoms or clusters.^[49] These results suggest that the reducing property of MOFs can be utilized to tune the chemical state of Co by engineering the composites with specific δ values.

The crystal structure of the final materials with various δ values was investigated by X-ray diffraction (XRD), as shown in Figure S3 (Supporting Information). No Co diffraction peaks are detected in CNS ($\delta = 0$) due to the absence of Co during the synthesis. When δ is changed to 1.0, the resulting Co@PGS exhibits the typical diffraction peaks of metallic Co. Further increasing δ to 1.5, $\text{Co}/\text{Co}_3\text{O}_4@PGS$ demonstrates the coexistence of metallic Co and spinel Co_3O_4 phases. Finally, when δ reaches a value of 2.0, only spinel Co_3O_4 reflections are observed in $\text{Co}_3\text{O}_4@PGS$. These results indicate that excessively reducing environments are created at relatively low δ ratios and thus any available Co^{2+} species are readily reduced to the metallic state. The reducing effect upon MOFs decomposition was weakened with relatively high δ ratios, which allows Co^{2+} species to remain as mixed or pure-spinel oxide states. This is the key to the chemical-state transformation of Co species that allows control of the final catalyst components.

Transmission electron microscopy (TEM) and high-resolution TEM (HRTEM) images of CNS display an amorphous structure with numerous micropores and no large mesopores (Figure S4, Supporting Information). In contrast, with the incorporation of Co^{2+} ($\delta = 1.0$) into Zn MOFs, the TEM and HRTEM images of Co@PGS show nanosheet-like configuration, where dark metallic Co is wrapped by porous graphitized shells (Figure S5a–c, Supporting Information), implying that the catalytic Co nanoparticles promote the graphitization of carbon.^[50,51] The initially generated Co nanoclusters on the carbon support tend to dissolve and grow into

nanosized particles due to the Ostwald ripening, leading to the formation of numerous graphitized holes (red arrows in Figure S5b, Supporting Information).^[52,53] The interconnected porous graphitized carbon plays a vital role in not only allowing intimate contact with Co nanoparticles, but also providing adequate open space and shortened diffusion channels for reactants and intermediates in the oxygen reactions. This configuration greatly facilitates both rapid charge transfer and mass transport in comparison to CNS, with the latter facilitating only zigzag channels along the interspace between nanosheets as illustrated in Figure S6 (Supporting Information).^[54,55] The scanning transmission electron microscopy (STEM) line-profile and electron energy loss spectroscopic (EELS) elemental maps acquired on a single particle of Co@PGS (Figure S5d, Supporting Information) further corroborate the sole existence of metallic Co.

Similarly, TEM imaging of $\text{Co}/\text{Co}_3\text{O}_4@PGS$ displays a sheet-like morphology (Figure 2a). The HRTEM image further illustrates that the Co-based particles with an average diameter of $\approx 10\text{ nm}$ are stitched within uniform porous graphitized shells (Figure 2b and Figure S7, Supporting Information). The multidirectional channels consisting of graphitized holes are also found throughout the TEM images of $\text{Co}/\text{Co}_3\text{O}_4@PGS$ (Figure 2c). It is worth mentioning that some morphological distortions are observed on the noncontinuous graphitic carbon framework (yellow circle in Figure 2c and Figure S8, Supporting Information), indicating the porous nature of the graphitized shells, which are expected to further improve the mass transfer to the $\text{Co}/\text{Co}_3\text{O}_4$ cores during the catalysis. More importantly, the defining “Janus” feature of $\text{Co}/\text{Co}_3\text{O}_4@PGS$ is the distinct double sets of interplanar spacing domains within the same particle denoted by e and f in Figure 2d. The lattice fringe with d -spacing of 0.177 nm is indexed to the (200) plane of metallic Co, while the other side with d -spacing of 0.199 nm corresponds to the (400) orientation of spinel Co_3O_4 (Figure 2d–f). The interpenetrating triphase of Co and the neighboring lattice of Co_3O_4 , highlighted by the dashed line in Figure 2d, is stitched in the graphitic carbon lattice and constructed by atomic-scale interfaces. Small pits marked by dashed circles are distributed near the interface domains (Figure 2d and Figure S9, Supporting Information), illustrating the formation of oxygen defects which can act as efficient active sites for oxygen

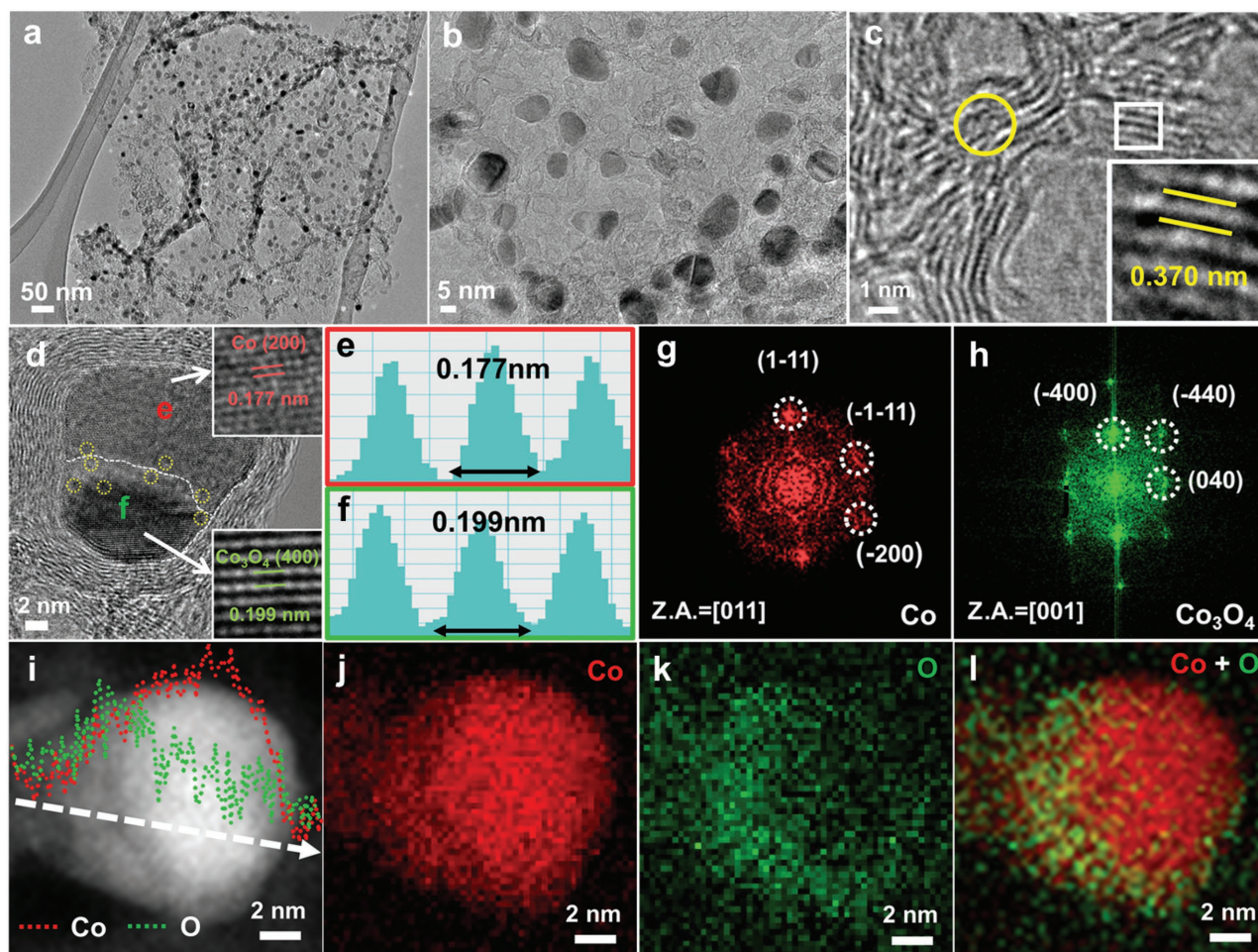


Figure 2. a,b) Overview TEM images of Co/Co₃O₄@PGS. c,d) HRTEM images of porous graphitized shells (PGS) and a single nanoparticle from Co/Co₃O₄@PGS. The intensity profiles of the *d*-spacing of the e) Co region in (d), f) Co₃O₄ region in (d). g,h) FFT patterns derived from the e and f regions in (d). i) Elemental distributions of Co and O in a single nanoparticle extracted from a STEM–EELS line profile. Aberration-corrected EELS elemental maps of j) Co, k) O, l) overlaid Co and O atoms.

catalysis.^[56] Also, the formation of the Schottky barrier between metallic Co and Co₃O₄ is favorable for charge separation.^[28] The numerous defects and Schottky barrier within the interfaces could serve as an atomic trap, thus effectively trapping more oxygen intermediates and enhancing charge transfer within the active sites. The fast Fourier transformation (FFT) patterns in Figure 2g,h taken from the e and f areas in Figure 2d further confirm the coexistence of metallic Co and spinel Co₃O₄. A STEM–EELS line-profile clearly demonstrates the elemental distribution of a typical Co/Co₃O₄ nanoparticle, identifying the asymmetric distribution of O atoms along the whole Janus nanoparticle (Figure 2i). The STEM–EELS elemental maps also support this Janus feature inside one nanoparticle (Figure 2j–l). When δ reaches a value of 2.0, the HRTEM image, STEM–EELS line-profile, and STEM–EELS elemental maps of Co₃O₄@PGS (Figure S10, Supporting Information) suggest the sole existence of spinel Co₃O₄. These results demonstrate that the Co-based interpenetrating triphase is successfully achieved by engineering the chemical state of the incorporated Co based on the redox interaction between Co²⁺ ions and Zn MOF nanosheets.

According to N₂ physisorption measurements, Co/Co₃O₄@PGS is estimated to possess a large specific surface area of 385 m² g⁻¹. As presented by the pore size distributions (Figure 3a), Co/Co₃O₄@PGS contains micropores with sizes less than 1 nm typically found in Zn MOFs (Figure S11, Supporting Information). Furthermore, the distinguishable hysteresis loop in the isotherm suggests the presence of mesopores in Co/Co₃O₄@PGS with a peak population of around 6 nm. In comparison, Co₃O₄@PGS manifests a much lower degree of mesoporosity, while fully reduced Co@PGS displays enhanced mesoporosity (Figure S12, Supporting Information). Finally, the macropores around 80 nm mainly originated from interlayer pores/spaces between sheets.^[55] These hierarchical pores of Co/Co₃O₄@PGS are favorable for exposing active sites and enriching the diffusion pathways for oxygen reactants.

Further insight into the electronic states of Co/Co₃O₄@PGS was gained by X-ray photoelectron spectroscopy (XPS). In comparison with the four peaks in the high-resolution N 1s XPS spectrum of CNS (Figure S13, Supporting Information), including pyridinic, pyrrolic, quaternary (or graphitic) N, and oxidized N, Co/Co₃O₄@PGS shows the similar four peaks

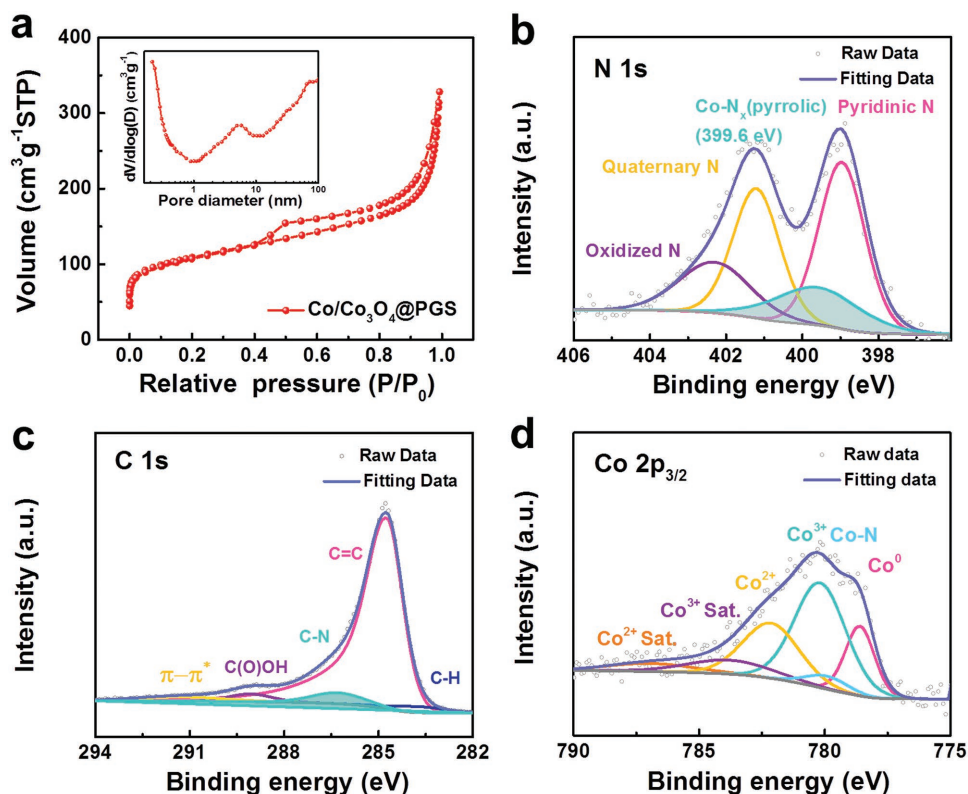


Figure 3. a) N_2 adsorption–desorption isotherm and pore size distribution, and the experimental and fitted high-resolution XPS spectra of b) N 1s, c) C 1s, d) Co $2p_{3/2}$ for $Co/Co_3O_4@PGS$.

except for a clear lower-energy shift of pyrrolic N (Figure 3b).^[57–59] Such phenomenon is attributed to the covalent bonds between Co and pyrrolic N, in which electrons are transferred from Co to N.^[60–62] A weak peak representing $Co-N_x$ bonds at 779.0 eV also demonstrates this electron transfer tendency (Figure 3d).^[63,64] Additionally, the peak at 399.6 eV ($Co-N_x$) disappeared after acid leaching of the Co/Co_3O_4 nanoparticles, accompanied by the formation of a new peak at 400.4 eV (pyrrolic-N) in $Co/Co_3O_4@PGS$ -acid, which further corroborates that the Co/Co_3O_4 nanoparticles are firmly rooted at the PGS surface through intimate covalent bonds between Co and N (Figure S13, Supporting Information). These bonds are formed during the vaporization of Zn in MOFs, which creates free N sites to act as the coordination site for Co.^[65] Such covalent bonds are also identified by a shift of the C–N peak to higher binding energy in the C 1s spectrum of $Co/Co_3O_4@PGS$ (Figure 3c) as compared with CNS (Figure S14, Supporting Information). Notably, no post-treatment in ammonia atmosphere was conducted to introduce N dopants, indicating the N-doped carbon matrix solely originates from the organic ligands of Zn MOFs. Figure 3d shows the Co $2p_{3/2}$ high resolution spectrum of $Co/Co_3O_4@PGS$. The peak deconvoluted at 778.6 eV is ascribed to metallic Co (Co^0), while the peaks at 780.2 and 781.9 eV reveal the presence of the Co_3O_4 phase.^[36] The Co and Co_3O_4 content derived from the XPS survey spectrum (Figure S15, Supporting Information) and Co $2p_{3/2}$ fitted measurements in the $Co/Co_3O_4@PGS$ hybrid is 6.2 and 13.7 wt%, respectively. The intensity of the Co^0 peak decreases from $Co@PGS$ to $Co_3O_4@PGS$ as

shown by their deconvoluted Co 2p spectra (Figure S16, Supporting Information), further indicating the gradual conversion of metallic Co to pure Co_3O_4 with increasing δ ratio. The relative atomic ratio of Co^{2+} and Co^{3+} in $Co/Co_3O_4@PGS$ (0.72) is higher than $Co_3O_4@PGS$ (0.5), indicating the higher number of oxygen defects in the former. These defects are further corroborated by high-resolution O 1s spectra which can be deconvoluted into five characteristic peaks for all as-synthesized catalysts, including oxygen bound to metal (lattice O), defect sites with low oxygen coordination (dissociative adsorbed O, O_{ad}), adsorbed molecular water (H_2O), and surface oxygen-containing groups (C–O and C=O) (Figure 4a–c).^[31,56] $Co/Co_3O_4@PGS$ presents the highest peak intensity ratio of O_{ad} among all samples, further illustrating the presence of more oxygen defects in $Co/Co_3O_4@PGS$ (Figure 4d). Both experimental and theoretical results have shown that oxygen defects formed by reduction promote electron injection to and extraction from O_2 and assure fast exchange kinetics of O^{2-}/OH^- for improvement of oxygen catalysis.^[1,11]

The electrical conductivities of synthesized sample are calculated from the I – V curves as shown in Figure S17 (Supporting Information). $Co/Co_3O_4@PGS$ exhibits a much higher conductivity of 8.41 S cm^{-1} than $Co@PGS$ (7.2 S cm^{-1}) and $Co_3O_4@PGS$ (3.05 S cm^{-1}), suggesting that its fast electron conduction is a result of the effective charge transfer between Co and Co_3O_4 at the interfaces.^[28] This is further evidenced by the temperature-dependent resistance curve of $Co/Co_3O_4@PGS$ presented in Figure S18 (Supporting Information). With elevated

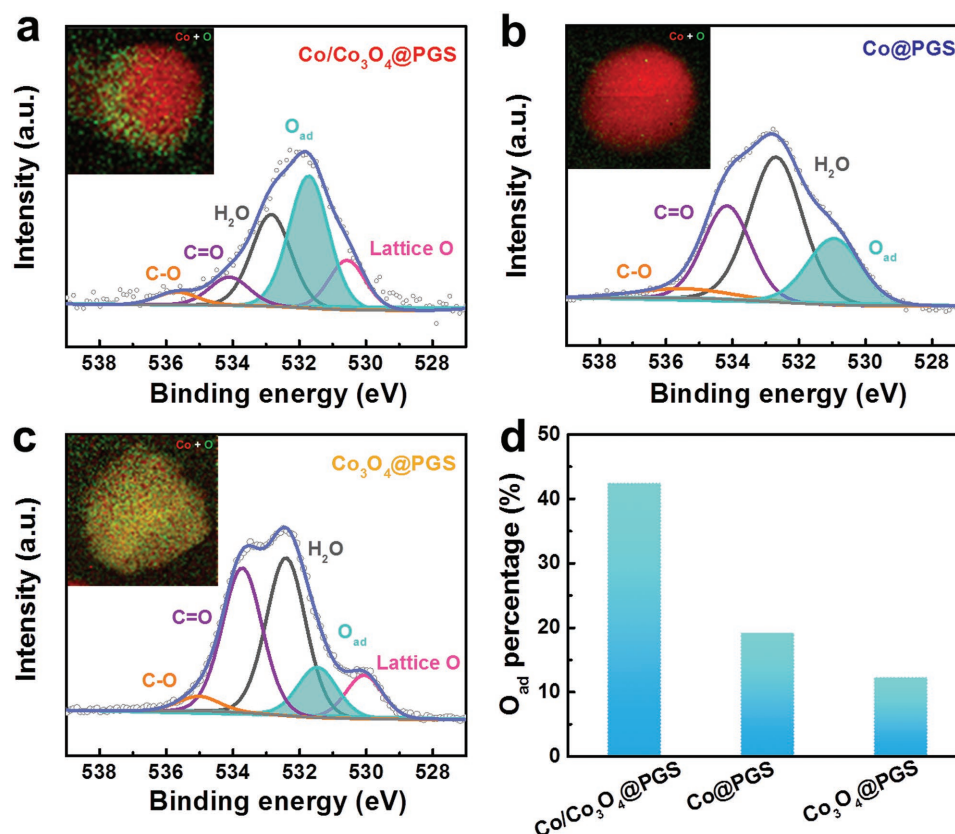


Figure 4. High-resolution O 1s XPS spectra of a) Co/Co₃O₄@PGS, b) Co@PGS, and c) Co₃O₄@PGS. d) O_{ad} percentages obtained from the high-resolution O1s XPS spectra.

temperature, the increase of electrical resistance unveils its metallic character, which is beneficial for the efficient transfer of electrons within the electroactive phases.

2.2. Electrochemical Evaluation

Linear sweep voltammetry (LSV) is adopted to evaluate ORR and OER activities of the catalysts as shown in **Figure 5**. CNS exhibits the worst bifunctional performance, as its amorphous and microporous structure hinders effective charge/mass transport. Among PGS-based catalysts, Co/Co₃O₄@PGS exhibits the highest onset potential (E_{onset}) of 0.97 V (vs reversible hydrogen electrode, RHE) in the ORR segment, indicating improved ORR kinetics compared to bare Co@PGS and Co₃O₄@PGS (Figure 5a). Additionally, Co/Co₃O₄@PGS shows the most positive ORR half-wave potential ($E_{\text{half-wave}}$) at 0.89 V. The outstanding electrocatalytic activity of Co/Co₃O₄@PGS is also demonstrated by its high diffusion-limited current densities (J_l) of 6.02 mA cm⁻², which is significantly larger than those of Co₃O₄@PGS (3.99 mA cm⁻²), Co@PGS (5.00 mA cm⁻²), and CNS (3.65 mA cm⁻²). The catalytic kinetics are assessed by electron-transfer numbers derived from Koutecky–Levich (K–L) plots at various potentials from 0.5 to 0.65 V. As shown in Figure S19 (Supporting Information), the electron-transfer number for Co/Co₃O₄@PGS is 4.0 on average, which is higher than those of its individual counterparts, signifying superior kinetics through a desirable four-electron

transfer pathway. Also, the smallest Tafel slope of 52.6 mV dec⁻¹ among the investigated materials indicates the most rapid ORR reaction kinetics of Co/Co₃O₄@PGS (Figure S20a, Supporting Information). More importantly, Co/Co₃O₄@PGS even surpasses the ORR benchmark catalyst with an $E_{\text{half-wave}}$ of 15 mV higher than that of Pt/C (Figure 5d).

As for OER activity, Co/Co₃O₄@PGS generates a current density of 10 mA cm⁻² at the potential ($E_{j=10}$) of 1.58 V as shown in Figure 5b. This potential is lower than those of Co@PGS, Co₃O₄@PGS, and CNS, and is also slightly lower than that of Ir/C ($E_{j=10}$ of 1.64 V) (Figure 5b,d). The lower Tafel slope of Co/Co₃O₄@PGS (76.1 mV dec⁻¹) in comparison to Ir/C (78.8 mV dec⁻¹) further confirms its optimized OER kinetics (Figure S20b, Supporting Information). The comprehensive bifunctional oxygen activity is assessed by the difference between ORR $E_{\text{half-wave}}$ and OER potential at 10 mA cm⁻², with a smaller value of ΔE ($\Delta E = E_{j=10} - E_{\text{half-wave}}$) indicating superior catalytic bifunctionality. As shown in Figure 5c and Table S1 (Supporting Information), Co/Co₃O₄@PGS exhibits the smallest ΔE of 0.69 V among the as-prepared catalysts. All these results imply that the unique Janus structure provides synergistic active sites and enhanced charge transfer, accounting for the enhancement in bifunctional activity. More importantly, the low ΔE of 0.69 V outperforms the most of well-developed bifunctional oxygen electrocatalysts containing cobalt oxide coupled with carbon materials outlined in Tables S2 and S3 (Supporting Information).

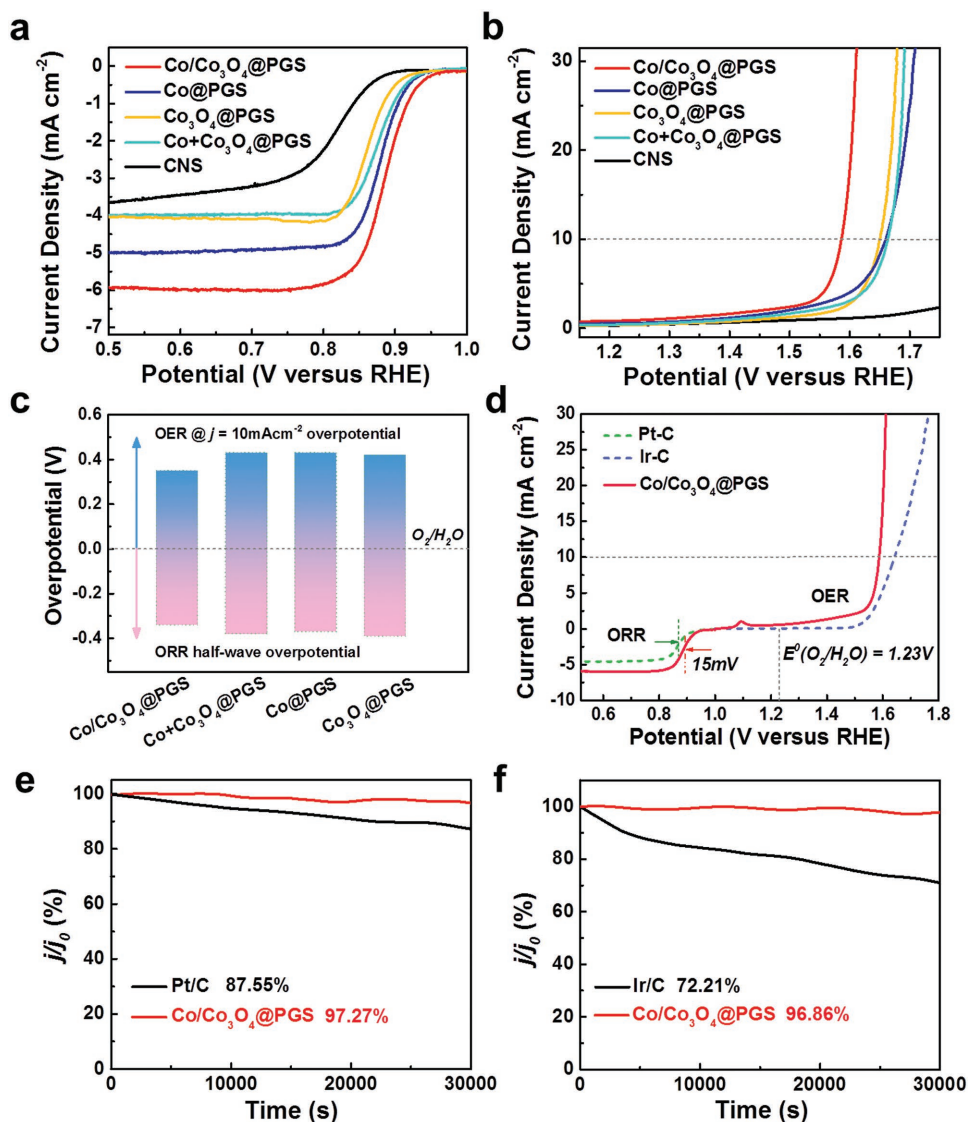


Figure 5. LSV of a) ORR and b) OER for Co/Co₃O₄@PGS, Co@PGS, Co₃O₄@PGS, Co+Co₃O₄@PGS, and CNS catalysts at 1600 rpm. c) Potential differences between the $E_{\text{half-wave}}$ of ORR and $E_{j=10}$ of OER for Co/Co₃O₄@PGS and other products. d) The entire LSV curves for bifunctional activities within the ORR and OER potential window of Co/Co₃O₄@PGS, Pt/C, and Ir/C at 1600 rpm. e) ORR chronoamperometric response of Co/Co₃O₄@PGS and Pt/C at a constant potential of 0.7 V. f) OER chronoamperometric response of Co/Co₃O₄@PGS and Ir/C at a constant potential of 1.6 V.

To further reveal the structural benefits of the interpenetrating interfaces in Co/Co₃O₄@PGS, the ORR and OER performances of the mechanical mixture of Co@PGS and Co₃O₄@PGS (denoted as Co+Co₃O₄@PGS) are measured. As expected, the Co/Co₃O₄@PGS with the interpenetrating phase within single Janus nanoparticles manifests higher bifunctional catalytic activity than Co+Co₃O₄@PGS with the segregated metal/oxide phases (Figure 5a–c), which confirms the synergistic effect arising from the newly designed Janus hybrid material. Specifically, the defect-rich interpenetrating interfaces act as atomic traps, allowing not only for the acceleration of charge transfer within each particle but also for the exceptional adsorption capability of oxygen-reactants. Moreover, the removal of the interpenetrating Co/Co₃O₄ nanoparticles by acid treatment leads to the drastically deteriorated bifunctional electrocatalytic

performance, indicating that the Co/Co₃O₄ cores are the main oxygen electrocatalytic active species (Figure S21, Supporting Information).

The durability of Co/Co₃O₄@PGS and noble-metal benchmarks was evaluated using the chronoamperometric response at 0.7 V for an extended period of 30 000 s. As shown in Figure 5e, Co/Co₃O₄@PGS retains 97.27% of the initial ORR current, outperforming 87.55% retention of Pt/C. Similarly, robust OER stability is also achieved by Co/Co₃O₄@PGS after 30 000 s at 1.6 V, with a high current retention of 96.86% that is superior to 72.21% of Ir/C (Figure 5f).

As a demonstration for practical application, rechargeable Zn–air batteries were assembled using a gas diffusion layer sprayed with Co/Co₃O₄@PGS as the air electrode (Figure 6a). A mixture of state-of-the-art commercial Pt/C and Ir/C with

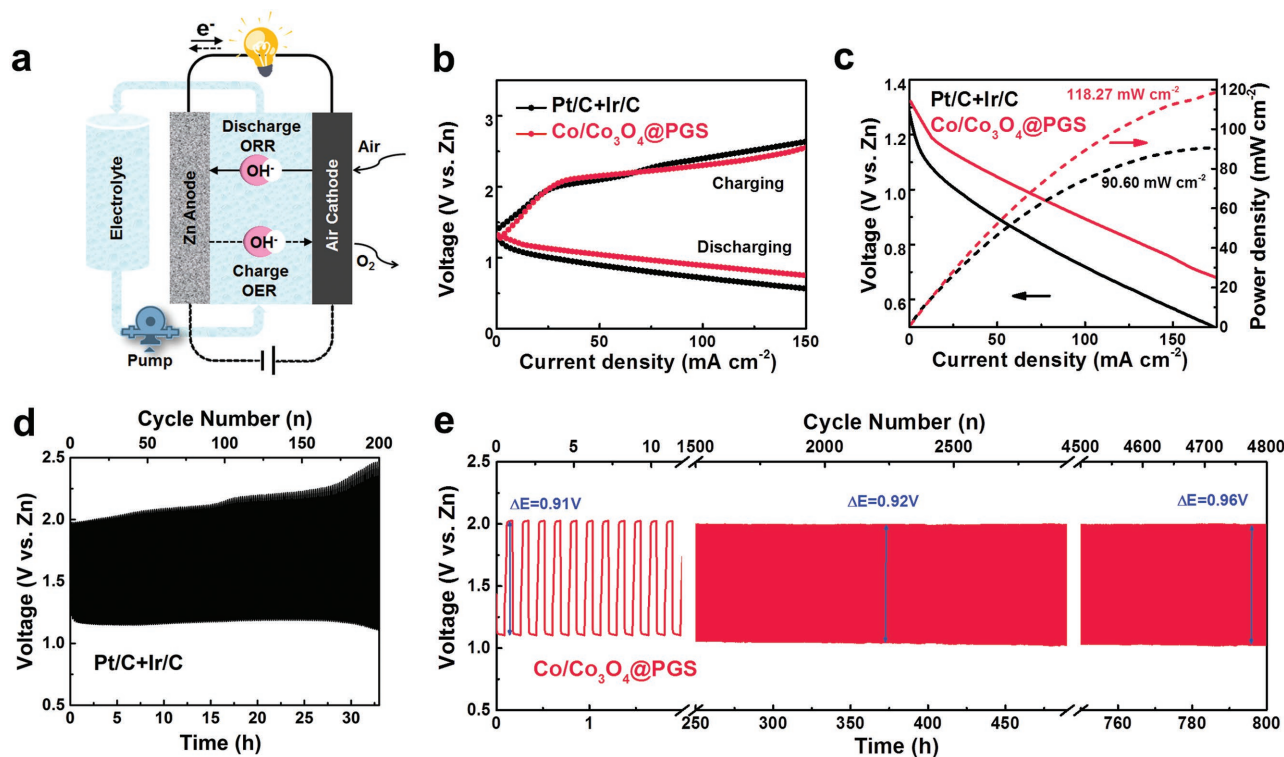


Figure 6. a) Schematic illustration of the flow Zn–air battery configuration. b) Charge and discharge polarization curves, c) discharge polarization curves and the corresponding power density plots for Zn–air battery with Co/Co₃O₄@PGS and Pt/C+Ir/C catalysts. Galvanostatic cycling stability of Zn–air battery with d) the coupled noble-metal Pt/C+Ir/C and e) Co/Co₃O₄@PGS catalysts at a current density of 10 mA cm⁻².

equal ratios was also tested in Zn–air batteries as the reference. As illustrated in Figure 6b, similar open circuit voltages of 1.45 V are provided by both Co/Co₃O₄@PGS and the reference, but Co/Co₃O₄@PGS demonstrates more ideal charge and discharge curves, especially at relatively high current densities. The smaller voltage gap between the ORR and OER curves of Co/Co₃O₄@PGS is attributed to the atomic trap between Co and Co₃O₄, resulting in efficient charge transfer and improved accessibility of electrolyte as well as oxygen species. This is also supported by the electrochemical impedance spectroscopy (EIS) spectra in Figure S22a (Supporting Information), in which Co/Co₃O₄@PGS is measured to have a lower charge transfer resistance of 1.4 Ω than the reference (2.5 Ω). Additionally, a power density of at least 118.27 mW cm⁻² is exhibited by Co/Co₃O₄@PGS (Figure 6c), which is higher than 90.60 mW cm⁻² for the reference.

The efficiency and long-term rechargeability of Co/Co₃O₄@PGS for Zn–air batteries is evaluated by galvanostatic charge–discharge at a current density of 10 mA cm⁻². As demonstrated in Figure 6d,e, Co/Co₃O₄@PGS provides a narrow charge–discharge gap of 0.91 V, which is comparable to the noble-metal reference. Most importantly, Co/Co₃O₄@PGS displays an excellent durability without noticeable voltage fading over 800 h (4800 cycles), while the Zn–air batteries prepared with Pt/C + Ir/C offer limited cyclability of less than 40 h. Particularly, the battery with Co/Co₃O₄@PGS as air cathode (Figure S22b, Supporting Information) is also capable of withstanding a high current density of 20 mA cm⁻², delivering a low voltage gap of

0.96 V for over 750 cycles. Undoubtedly, the excellent long-term rechargeability can be attributed to the hybrid structure, where Janus nanoparticles stitched in the porous graphitized support provide enhanced stability through reinforced chemically covalent Co–N.^[21] To investigate the structural evolution upon cycling, SEM and TEM observations were performed on the Co/Co₃O₄@PGS electrode cycled after 800 h (Figure S23a,b, Supporting Information), which indicates the overall integrity of the 2D structures was not affected during the cycling. Co-based nanoparticles are observed still well anchored on the PGS without obvious aggregation or detachment, which confirms the robustness of the hybrid structure after long periods of alternating redox reactions. Additionally, Figure S23c in the Supporting Information shows that the Co/Co₃O₄ particle does retain its asymmetric crystal and chemical structures after cycling. The Zn–air battery with such long-lasting rechargeable stability over this time-scale is evidently superior to bifunctional oxygen electrocatalysts reported thus far (Table S3, Supporting Information).

In summary, superior bifunctional electrocatalytic activity and long-lasting stability are realized by Co/Co₃O₄@PGS, surpassing both ORR and OER benchmarks. The superior electrochemical performance can be attributed to the following reasons: (i) the defect-rich interfaces introduced by phase interpenetration between metallic Co and spinel Co₃O₄ generate numerous atomic traps that capture and immobilize oxygen-reactants toward catalytic sites; (ii) the construction of highly conductive networks accelerates both surface and bulk charge

transfer throughout the electrocatalyst; (iii) the pores of PGS favor the diffusion of the reactants, allowing efficient mass transfer; (iv) the formation of robust covalent bonds between Co and N precludes the potential for exfoliation of the structure.

3. Conclusion

In this work, a unique hybrid comprised of interpenetrating Co and Co₃O₄ nanoparticles stitched in a porous graphitized shell is designed and successfully synthesized via ionic exchange and redox reaction between Co²⁺ ions and Zn MOF nanosheets. The hybrid bifunctional electrocatalyst surpasses noble-metal benchmarks for both ORR (a half-wave potential 15 mV higher than Pt/C) and OER (an overpotential at 10 mA cm⁻² 60 mV lower than Ir/C). When integrated within an air electrode, the hybrid catalyst is demonstrated to show exceptionally high stability with little voltage fading over 800 h at 10 mA cm⁻², which to our knowledge is a new record among reported rechargeable Zn–air batteries. The excellent electrochemical performance is enabled by the combination of numerous and effective catalytic sites and favorable charge/mass transfer provided by the specially designed hybrid with interpenetrating multiphase and hierarchical porosity. These findings pave a new way for designing the next generation of electrocatalysts.

4. Experimental Section

Chemicals: 2-Methylimidazole (99%, Analytical grade), zinc nitrite hexahydrate (99%, Analytical grade), zinc acetate tetrahydrate (99%, Analytical grade), cobalt nitrite hexahydrate (99%, Analytical grade), potassium hydroxide (85%, Analytical grade), and ethanol (99.9%, anhydrous) were purchased from Sigma-Aldrich. Nafion dispersion (5 wt% in ethanol) was bought from Ion Power. All chemicals were used without further purification. The deionized water (18 M Ω) was obtained from a Millipore System.

Synthesis of Zn MOFs Nanosheets: 0.33 g Zn(NO₃)₂·6H₂O was first dissolved in 90 mL deionized water; the solution was then added to another 90 mL deionized water containing 0.985 g 2-methylimidazole under vigorous stirring and allowed to react for 24 h at room temperature. After that, the white product, labeled as Zn MOF nanosheets, was washed by deionized water and dried in ambient air.

Synthesis of CNS, Co@PGS, Co/Co₃O₄@PGS, Co₃O₄@PGS, Co+Co₃O₄@PGS, and Co/Co₃O₄@PGS-acid: The CNS, Co@PGS, Co/Co₃O₄@PGS, and Co₃O₄@PGS were prepared using the same procedure but different weight ratios of as-prepared Zn MOF nanosheets to Co(NO₃)₂·6H₂O from 0, 1, 1.5, or 2, respectively. In a typical synthesis of Co/Co₃O₄@PGS, the as-prepared Zn MOF nanosheets (0.08 g) were added into 25 mL ethanol containing 0.12 g of Co(NO₃)₂·6H₂O. The resulting solution was sonicated and stirred for 30 min. After this, the solvent was vaporized at 80 °C in an oven and the obtained pink powder was labeled as Zn/Co MOFs-Co(NO₃)₂. Then, the Zn/Co MOFs-Co(NO₃)₂ precursor was annealed at 920 °C for 2 h with a heating rate of 2 °C min⁻¹ under Ar flow in a tube furnace. After cooling to room temperature, the obtained black product was named Co/Co₃O₄@PGS. The Co+Co₃O₄@PGS was obtained by mechanically mixing the as-synthesized Co@PGS and Co₃O₄@PGS with a molar ratio of 1:1. The Co/Co₃O₄@PGS-acid was obtained from the acid-leaching of Co/Co₃O₄@PGS in 2.0 M HCl at 80 °C for 10 h. It was then washed by deionized water and ethanol, and dried in ambient air.

Fabrication of Zn–Air Battery: Stainless steel meshes and copper foil were used as current collectors for the air cathodes and Zn anodes, respectively. The Co/Co₃O₄@PGS nanocomposites were used as

the bifunctional electroactive material to fabricate the air cathode. Homogeneous catalyst ink consisting of nanocomposites, ionomer (Nafion solution, 5 wt%) and ethanol was sprayed onto a gas diffusion layer (Ion Power Inc., 35 BC) with a catalyst loading of 0.9 mg cm⁻². As a reference, commercial state-of-art 28.8 wt% Ir/C and Pt/C catalysts with the same loading were prepared using the same method. The air cathode was then paired with a Zn plate anode and assembled in a battery prototype filled with a solution of 6.0 M KOH and 0.20 M Zn(CH₃COO)₂.

Materials Characterization: TEM images were taken using a Hitachi 7600 microscope operated at 120 kV. HRTEM, HAADF-STEM, and EELS analyses were performed using a Hitachi aberration-corrected STEM HD-2700C. An electron probe diameter of 1.3 Å with a convergence angle of 28 mrad was used. The STEM–EELS 2D maps and EELS line scans were collected with a pixel time of 0.02 s using a Gatan Enfina-ER detector. XRD patterns were obtained by a Bruker AXS D8 Advance powder X-ray diffractometer equipped with a Cu K α radiation source ($\lambda = 1.5406$ Å) and a graphite monochromator. XPS measurements were carried out by a Thermal Scientific K-Alpha XPS spectrometer. The pore structure was investigated by N₂ adsorption–desorption measurements on a Brunauer–Emmett–Teller surface area analyzer (Quantachrome Instruments QuadraSorb SI4) and a Barrett–Joyner–Halenda model was used to obtain pore size distribution. The TGA was conducted on a TA instrument Q500.

Electrochemical Measurement: The electrochemical measurements were performed in a three-electrode system with an electrochemical workstation (Biologic VMP-3). The electrocatalytic performances for ORR and OER were measured by a rotating disk electrode in a three-electrode cell at standard temperature and pressure conditions. The three-electrode system contains a glassy carbon electrode (GC; 5 mm in diameter), a graphite rod, and a RHE as the working, counter, and reference electrodes, respectively. The catalyst ink was prepared by mixing 4 mg of the catalyst in 1000 μ L of ethanol containing 0.15 wt% Nafion dispersion, followed by ultrasonication for 1 h to obtain a homogeneous ink. Then 15 μ L of the as-prepared ink was dropped onto the GC surface to give a catalyst loading of 0.3 mg cm⁻² for all the developed catalysts. The commercial Pt/C (28.8 wt% Pt) and Ir/C (20 wt% Ir) catalysts were used as the reference materials and their catalytic performances were measured with same catalyst loading of 0.3 mg cm⁻². All the measurements were carried out in 0.1 M KOH solution, where O₂ or N₂ gas was purged for 30 min before ORR or OER measurements, respectively. The LSV measurements were performed from 1.0 to 0.1 V at different rotation speeds for ORR and from 1.0 to 1.8 V at a rotation speed of 1600 rpm for OER with scan rate of 10 mV s⁻¹. ORR and OER polarization curves were corrected by IR-compensation in 0.1 M KOH solution, where the resistance (40 Ω) is determined by the high-frequency intercept from the Nyquist plot acquired from EIS. Capacitive background currents were subtracted for ORR and OER polarization curves during cyclic voltammetry measurements in N₂-saturated KOH solution. The stability studies on the half-cell reactions (ORR and OER separately) was primarily assessed by chronoamperometric measurements at a given constant potential for 30 000 s. Galvanostatic discharge and charge cycling of the Zn–air batteries was performed through a recurrent galvanostatic pulse method at a current density of 10 or 20 mA cm⁻² with 10 min per cycle. These galvanostatic charge/discharge curves were recorded using a LAND battery testing station (CT2001A) at room temperature. Polarization data was collected using the galvanodynamic method at a scan rate of 1.0 mA s⁻¹ with cut-off voltages of 0.5 V for the discharge curves and 2.5 V for the charge curves. EIS was performed with a frequency ranging from 100 kHz to 0.1 Hz with potential amplitude of 50 mV.

Supporting Information

Supporting Information is available from the Wiley Online Library or from the author.

Acknowledgements

This work was financially supported by the Natural Sciences and Engineering Research Council of Canada (NSERC), the National Natural Science Foundation (21573083), the University of Waterloo, and the Waterloo Institute for Nanotechnology and the 111 Project (No. D17007) and the Strategic Priority Research Program of the Chinese Academy of Sciences (No. XDA09040101). The authors also thank the support of the University of Chinese Academy of Sciences (UCAS) Joint Ph.D. Training Program.

Conflict of Interest

The authors declare no conflict of interest.

Keywords

bifunctional electrocatalysts, interpenetrating phases, metal–organic frameworks, Zn–air batteries

Received: October 18, 2017

Revised: December 11, 2017

Published online: January 31, 2018

- [1] J. Fu, F. M. Hassan, C. Zhong, J. Lu, H. Liu, A. Yu, Z. Chen, *Adv. Mater.* **2017**, *29*, 1702526.
- [2] J. Fu, Z. P. Cano, M. G. Park, A. Yu, M. Fowler, Z. Chen, *Adv. Mater.* **2017**, *29*, 1604685.
- [3] J.-S. Lee, S. Tai Kim, R. Cao, N.-S. Choi, M. Liu, K. T. Lee, J. Cho, *Adv. Energy Mater.* **2011**, *1*, 34.
- [4] J. Fu, F. M. Hassan, J. Li, D. U. Lee, A. R. Ghannoum, G. Lui, M. A. Hoque, Z. Chen, *Adv. Mater.* **2016**, *28*, 6421.
- [5] Y. Li, H. Dai, *Chem. Soc. Rev.* **2014**, *43*, 5257.
- [6] R. Cao, J. S. Lee, M. Liu, J. Cho, *Adv. Energy Mater.* **2012**, *2*, 816.
- [7] Y. Li, J. Lu, *ACS Energy Lett.* **2017**, *2*, 1370.
- [8] J.-S. Lee, T. Lee, H.-K. Song, J. Cho, B.-S. Kim, *Energy Environ. Sci.* **2011**, *4*, 4148.
- [9] Y. Li, M. Gong, Y. Liang, J. Feng, J.-E. Kim, H. Wang, G. Hong, B. Zhang, H. Dai, *Nat. Commun.* **2013**, *4*, 1805.
- [10] J.-I. Jung, M. Risch, S. Park, M. G. Kim, G. Nam, H.-Y. Jeong, Y. Shao-Horn, J. Cho, *Energy Environ. Sci.* **2016**, *9*, 176.
- [11] J. Park, M. Risch, G. Nam, M. Park, T. J. Shin, S. Park, M. G. Kim, Y. Shao-Horn, J. Cho, *Energy Environ. Sci.* **2017**, *10*, 129.
- [12] B. Y. Guan, L. Yu, X. W. Lou, *Energy Environ. Sci.* **2016**, *9*, 3092.
- [13] D. U. Lee, P. Xu, Z. P. Cano, A. G. Kashkooli, M. G. Park, Z. Chen, *J. Mater. Chem. A* **2016**, *4*, 7107.
- [14] Z. Chen, A. Yu, D. Higgins, H. Li, H. Wang, Z. Chen, *Nano Lett.* **2012**, *12*, 1946.
- [15] Q. Li, H. Pan, D. Higgins, R. Cao, G. Zhang, H. Lv, K. Wu, J. Cho, *G. Wu, Small* **2015**, *11*, 1443.
- [16] C. Li, X. Han, F. Cheng, Y. Hu, C. Chen, J. Chen, *Nat. Commun.* **2015**, *6*, 7345.
- [17] X. Liu, M. Park, M. G. Kim, S. Gupta, X. Wang, G. Wu, J. Cho, *Nano Energy* **2016**, *20*, 315.
- [18] F. Meng, H. Zhong, D. Bao, J. Yan, X. Zhang, *J. Am. Chem. Soc.* **2016**, *138*, 10226.
- [19] J. Jiang, Y. Li, J. Liu, X. Huang, C. Yuan, X. W. Lou, *Adv. Mater.* **2012**, *24*, 5166.
- [20] M. Wang, M. Lin, J. Li, L. Huang, Z. Zhuang, C. Lin, L. Zhou, L. Mai, *Chem. Commun.* **2017**, *53*, 8372.
- [21] G. Li, X. Wang, J. Fu, J. Li, M. G. Park, Y. Zhang, G. Lui, Z. Chen, *Angew. Chem., Int. Ed.* **2016**, *55*, 4977.
- [22] X. Chen, B. Liu, C. Zhong, Z. Liu, J. Liu, L. Ma, Y. Deng, X. Han, T. Wu, W. Hu, J. Lu, *Adv. Energy Mater.* **2017**, *7*, 1700779.
- [23] M. G. Park, D. U. Lee, M. H. Seo, Z. P. Cano, Z. Chen, *Small* **2016**, *12*, 2707.
- [24] D. U. Lee, M. G. Park, H. W. Park, M. H. Seo, X. Wang, Z. Chen, *ChemSusChem* **2015**, *8*, 3129.
- [25] Y. Liang, Y. Li, H. Wang, J. Zhou, J. Wang, T. Regier, H. Dai, *Nat. Mater.* **2011**, *10*, 780.
- [26] F. Cheng, J. Shen, B. Peng, Y. Pan, Z. Tao, J. Chen, *Nat. Chem.* **2011**, *3*, 79.
- [27] Y. Liang, Y. Li, H. Wang, H. Dai, *J. Am. Chem. Soc.* **2013**, *135*, 2013.
- [28] A. Ajaj, J. Masa, C. Rösler, W. Xia, P. Weide, A. J. Botz, R. A. Fischer, W. Schuhmann, M. Muhler, *Angew. Chem., Int. Ed.* **2016**, *55*, 4087.
- [29] Y. Liang, H. Wang, J. Zhou, Y. Li, J. Wang, T. Regier, H. Dai, *J. Am. Chem. Soc.* **2012**, *134*, 3517.
- [30] G. Zhang, B. Y. Xia, X. Wang, X. W. Lou, *Adv. Mater.* **2014**, *26*, 2408.
- [31] D. U. Lee, J. Li, M. G. Park, M. H. Seo, W. Ahn, I. Stadelmann, L. Ricardez-Sandoval, Z. Chen, *ChemSusChem* **2017**, *10*, 2258.
- [32] Z.-L. Wang, D. Xu, J.-J. Xu, X.-B. Zhang, *Chem. Soc. Rev.* **2014**, *43*, 7746.
- [33] F. Wang, P. He, Y. Li, T. A. Shifa, Y. Deng, K. Liu, Q. Wang, F. Wang, Y. Wen, Z. Wang, Zhan, Xueying, L. Sun, J. He, *Adv. Funct. Mater.* **2017**, *27*, 1605802.
- [34] Y. Hou, M. Qiu, G. Nam, M.-G. Kim, T. Zhang, K. Liu, X. Zhuang, J. Cho, C. Yuan, X. Feng, *Nano Lett.* **2017**, *17*, 4202.
- [35] Z. Wu, J. Wang, L. Han, R. Lin, H. Liu, H. L. Xin, D. Wang, *Nanoscale* **2016**, *8*, 4681.
- [36] J. Yu, G. Chen, J. Sunarso, Y. Zhu, R. Ran, Z. Zhu, W. Zhou, Z. Shao, *Adv. Sci.* **2016**, *3*, 1600060.
- [37] B. Y. Xia, Y. Yan, N. Li, H. B. Wu, X. W. Lou, X. Wang, *Nat. Energy* **2016**, *1*, 15006.
- [38] H. Zhang, J. Nai, L. Yu, X. W. Lou, *Joule* **2017**, *1*, 77.
- [39] B. Y. Guan, L. Yu, X. W. Lou, *Adv. Sci.* **2017**, *4*, 1700247.
- [40] Y. Hao, Y. Xu, J. Liu, X. Sun, *J. Mater. Chem. A* **2017**, *5*, 5594.
- [41] H. Hu, L. Han, M. Yu, Z. Wang, X. W. D. Lou, *Energy Environ. Sci.* **2016**, *9*, 107.
- [42] J. Tang, R. R. Salunkhe, J. Liu, N. L. Torad, M. Imura, S. Furukawa, Y. Yamauchi, *J. Am. Chem. Soc.* **2015**, *137*, 1572.
- [43] L.-F. Chen, Y. Lu, L. Yu, X. W. Lou, *Energy Environ. Sci.* **2017**, *10*, 1707.
- [44] S. Zhao, Y. Wang, J. Dong, C.-T. He, H. Yin, P. An, K. Zhao, X. Zhang, C. Gao, L. Zhang, J. Lv, J. Wang, J. Zhang, A. Khattak, N. Khan, Z. Wei, J. Zhang, S. Liu, Z. Tang, *Nat. Energy* **2016**, *1*, 2016184.
- [45] Z. Zhang, Y. Chen, S. He, J. Zhang, X. Xu, Y. Yang, F. Nosheen, F. Saleem, W. He, X. Wang, *Angew. Chem., Int. Ed.* **2014**, *126*, 12725.
- [46] E. Shamsaei, Z.-X. Low, X. Lin, A. Mayahi, H. Liu, X. Zhang, J. Z. Liu, H. Wang, *Chem. Commun.* **2015**, *51*, 11474.
- [47] R. Soltani, A. Shahvar, M. Dinari, M. Saraji, *Ultrason. Sonochem.* **2018**, *40*, 395.
- [48] C. Ehrhardt, M. Gjikaj, W. Brockner, *Thermochim. Acta* **2005**, *432*, 36.
- [49] Y. Jiang, H. Liu, X. Tan, L. Guo, J. Zhang, S. Liu, Y. Guo, J. Zhang, H. Wang, W. Chu, *ACS Appl. Mater. Interfaces* **2017**, *9*, 25239.
- [50] J. Meng, C. Niu, L. Xu, J. Li, X. Liu, X. Wang, Y. Wu, X. Xu, W. Chen, Q. Li, Z. Zhu, D. Zhao, L. Mai, *J. Am. Chem. Soc.* **2017**, *139*, 8212.
- [51] Y. M. Chen, L. Yu, X. W. Lou, *Angew. Chem., Int. Ed.* **2016**, *55*, 5990.
- [52] X. W. Lou, C. Yuan, E. Rhoades, Q. Zhang, L. A. Archer, *Adv. Funct. Mater.* **2006**, *16*, 1679.
- [53] T. W. Hansen, A. T. DeLaRiva, S. R. Challa, A. K. Datye, *Acc. Chem. Res.* **2013**, *46*, 1720.
- [54] Y. Xu, Z. Lin, X. Zhong, X. Huang, N. O. Weiss, Y. Huang, X. Duan, *Nat. Commun.* **2014**, *5*, 4554.

- [55] D. Zhou, Y. Cui, P.-W. Xiao, M.-Y. Jiang, B.-H. Han, *Nat. Commun.* **2014**, *5*, 4716.
- [56] M. Yu, Z. Wang, C. Hou, Z. Wang, C. Liang, C. Zhao, Y. Tong, X. Lu, S. Yang, *Adv. Mater.* **2017**, *29*, 1602868.
- [57] L. Dai, Y. Xue, L. Qu, H.-J. Choi, J.-B. Baek, *Chem. Rev.* **2015**, *115*, 4823.
- [58] H. Wang, T. Maiyalagan, X. Wang, *ACS Catal.* **2012**, *2*, 781.
- [59] H. B. Yang, J. Miao, S.-F. Hung, J. Chen, H. B. Tao, X. Wang, L. Zhang, R. Chen, J. Gao, H. M. Chen, L. Dai, B. Liu, *Sci. Adv.* **2016**, *2*, e1501122.
- [60] A. Morozan, P. Jégou, B. Jusselme, S. Palacin, *Phys. Chem. Chem. Phys.* **2011**, *13*, 21600.
- [61] K. Artyushkova, A. Serov, S. Rojas-Carbonell, P. Atanassov, *J. Phys. Chem. C* **2015**, *119*, 25917.
- [62] Y. Qian, Z. Liu, H. Zhang, P. Wu, C. Cai, *ACS Appl. Mater. Interfaces* **2016**, *8*, 32875.
- [63] J. Masa, W. Xia, I. Sinev, A. Zhao, Z. Sun, S. Grütze, P. Weide, M. Muhler, W. Schuhmann, *Angew. Chem., Int. Ed.* **2014**, *53*, 8508.
- [64] T. Okada, M. Gokita, M. Yuasa, I. Sekine, *J. Electrochem. Soc.* **1998**, *145*, 815.
- [65] P. Yin, T. Yao, Y. Wu, L. Zheng, Y. Lin, W. Liu, H. Ju, J. Zhu, X. Hong, Z. Deng, G. Zhou, S. Wei, Y. Li, *Angew. Chem., Int. Ed.* **2016**, *55*, 10800.